ECCOMAS Congress 2016
VII European Congress on Computational Methods in Applied Sciences and Engineering
M. Papadrakakis, V. Papadopoulos, G. Stefanou, V. Plevris (eds.)
Crete Island, Greece, 5–10 June 2016

DISCONTINUOUS GALERKIN SOLUTION OF THE REYNOLDS-AVERAGED NAVIER–STOKES AND K_L-K_T-$\tilde{\omega}$ TRANSITION MODEL EQUATIONS

A. Bassi[1], **A. Colombo**[1], **A. Ghidoni**[2], **M. Lorini**[2], **and G. Noventa**[2]

[1] Dipartimento di Ingegneria Industriale, Università di Bergamo
Viale Marconi 5, 24044 Dalmine (BG), Italy
e-mail: {francesco.bassi,alessandro.colombo}@unibg.it

[2] Dipartimento di Ingegneria Meccanica e Inustriale, Università di Brescia
via Branze 38, 25123 Brescia, Italy
e-mail: {antonio.ghidoni,m.lorini006,g.noventa002}@unibs.it

Keywords: RANS Equations, DG Method, Transition Modeling, local model, laminar kinetic energy.

Abstract. *Transition modelling represents a key ingredient to improve the performances of modern turbomachinery, affecting losses and the heat-transfer phenomenon. In this paper the transition model proposed by Walters [3] was considered. It is based on the k-ω formulation with the addition of a third transport equation (k_L equation), which allows predicting the magnitude of low-frequency velocity fluctuations in the pre-transitional boundary layer. The model was implemented into a parallel high-order accurate Discontinuous Galerkin code, named MIGALE, which allows to solve the Reynolds averaged Navier-Stokes (RANS) equations coupled with the k-$\widetilde{\omega}$ ($\tilde{\omega} = \log(\omega)$) turbulence model. The model was applied to two test cases, namely the flat plate (T3A and T3B configuration) and the T106A turbine cascade. Results obtained with and without transition model were compared with experimental data.*

1 INTRODUCTION

In the last decade, Computational Fluid Dynamic (CFD) has become a tool commonly adopted for industrial analysis and design. This wide spread can be partially explained by the development of reliable and robust turbulence models. However, these turbulence models are very well suited for high Reynolds number flows, whereas for low Reynolds numbers flows, where a large part of the boundary layer is laminar or transitional, they can provide wrong results. Therefore, the transition modeling represents a key ingredient to improve the prediction capabilities of standard RANS solvers. Different methods have been proposed in the finite volume context to predict the laminar-turbulent transition [1, 2, 3], but, according to the literature, there was only an attempt to couple a non-local transition model [17] with a high-order method. In this paper the local transition model proposed by Walters [3] was considered. The model is based on the k-ω formulation with the addition of a third transport equation (k_L equation), which allows predicting the magnitude of low-frequency velocity fluctuations in the pre-transitional boundary layer. The closure of the model is based on a phenomenological (*i.e.* physics-based) rather than a purely empirical approach. The model was implemented into a parallel high-order accurate Discontinuous Galerkin (DG) code, named MIGALE [4, 5], which allows solving the RANS equations coupled with the k-$\widetilde{\omega}$ turbulence model. The objective of this work is to assess the capability of high-order DG methods in accurately computing transitional flows on two benchmark testcases, i.e. the transitional flow around a flat plate (T3A and T3B configurations) and through the T106A turbine cascade, comparing high-order results with available numerical and experimental data.

2 GOVERNING EQUATIONS

The complete set of RANS and k_L-k_T-$\widetilde{\omega}$ model equations can be written as

$$\frac{\partial \rho}{\partial t} + \frac{\partial}{\partial x_j}(\rho u_j) = 0 \ , \tag{1}$$

$$\frac{\partial}{\partial t}\left(\rho u_i\right) + \frac{\partial}{\partial x_j}(\rho u_j u_i) = -\frac{\partial p}{\partial x_i} + \frac{\partial \widehat{\tau}_{ji}}{\partial x_j} \ , \tag{2}$$

$$\frac{\partial}{\partial t}(\rho E) + \frac{\partial}{\partial x_j}(\rho u_j H) = \frac{\partial}{\partial x_j}\left[u_i \widehat{\tau}_{ij} - \widehat{q}_j\right] - \rho(P_{k_T} - \overline{k}_T \widetilde{\omega}) \ , \tag{3}$$

$$\begin{aligned}\frac{\partial}{\partial t}(\rho k_T) + \frac{\partial}{\partial x_j}(\rho u_j k_T) =& \frac{\partial}{\partial x_j}\left[\left(\mu + \frac{\rho \alpha_T}{\sigma_k}\right)\frac{\partial k_T}{\partial x_j}\right] \\ &+ \rho\left(P_{k_T} + R_{BP} + R_{NAT} - \overline{k}_T\widetilde{\omega} - D_T\right) \ ,\end{aligned} \tag{4}$$

$$\frac{\partial}{\partial t}(\rho k_L) + \frac{\partial}{\partial x_j}(\rho u_j k_L) = \frac{\partial}{\partial x_j}\left[\mu \frac{\partial k_L}{\partial x_j}\right] + \rho\left(P_{k_L} - R_{BP} - R_{NAT} - D_L\right) \ , \tag{5}$$

$$\begin{aligned}\frac{\partial}{\partial t}(\rho\widetilde{\omega}) + \frac{\partial}{\partial x_j}(\rho u_j \widetilde{\omega}) = \frac{\partial}{\partial x_j}\left[\left(\mu + \frac{\rho\alpha_T}{\sigma_\omega}\right)\frac{\partial \widetilde{\omega}}{\partial x_j}\right] + \rho\left[\left(\frac{C_{\omega R}}{f_W} - 1\right)\frac{\widetilde{\omega}}{\overline{k}_T}\left(R_{BP} + R_{NAT}\right)\right. \\ \left. + C_{\omega 1}\frac{\widetilde{\omega}}{\overline{k}_T}P_{k_T} - f_2\widetilde{\omega}^2 + P_{BL}\right] + \left(\mu + \frac{\rho\alpha_T}{\sigma_\omega}\right)\frac{\partial\widetilde{\omega}}{\partial x_k}\frac{\partial\widetilde{\omega}}{\partial x_k} \ ,\end{aligned} \tag{6}$$

where u_i is the absolute velocity.

The total energy, the total enthalpy, the pressure, the turbulent and total stress tensors, the heat flux vector, the eddy viscosity and the limited value of laminar and turbulent kinetic energy are given by

$$E = \hat{e} + u_k u_k/2, \tag{7}$$
$$H = h + u_k u_k/2, \tag{8}$$
$$p = (\gamma - 1)\rho \left(E - u_k u_k/2\right), \tag{9}$$
$$\tau_{ij} = 2\mu_t \left[S_{ij} - \frac{1}{3}\frac{\partial u_k}{\partial x_k}\delta_{ij}\right] - \frac{2}{3}\rho \overline{k}_T \delta_{ij}, \tag{10}$$
$$\widehat{\tau}_{ij} = 2\mu \left[S_{ij} - \frac{1}{3}\frac{\partial u_k}{\partial x_k}\delta_{ij}\right] + \tau_{ij}, \tag{11}$$
$$\widehat{q}_j = -\left(\frac{\mu}{\mathrm{Pr}} + \rho\alpha_\theta\right)\frac{\partial h}{\partial x_j}, \tag{12}$$
$$\mu_t = \rho\left(\nu_{T,s} + \nu_{T,l}\right), \tag{13}$$
$$\overline{k}_T = \max\left(0, k_T\right), \quad \overline{k}_L = \max\left(0, k_L\right), \tag{14}$$

where $\hat{e}$ is the internal energy, h the enthalpy, γ the ratio of gas specific heats, Pr the molecular Prandtl number and

$$S_{ij} = \frac{1}{2}\left(\frac{\partial u_i}{\partial x_j} + \frac{\partial u_j}{\partial x_i}\right)$$

is the mean strain-rate tensor.

The turbulence model was implemented using $\widetilde{\omega} = \log(\omega)$ instead of ω, limiting the values of k_T and k_L. At solid walls the homogeneous Neumann condition for the specific dissipation rate $\partial\widetilde{\omega}/\partial n = 0$ is prescribed.

Furthermore, due to the no-slip condition, the velocity is set to zero. Since the velocity is equal to zero, the kinetic energy at the wall must also reduce to zero. Therefore, turbulent and laminar kinetic energy are set to zero at the wall.

2.1 TRANSITION MODEL

The transition model considered in this work (see Eqs. 4, 5 and 6) is based on the model proposed by Walters [3]. This model includes several damping functions for the different physical phenomena observed (such as shear sheltering and wall reflection), which require empirically determined constants. However, the amount of empiricism necessary is still significantly less if compared to correlation-based intermittency models.

The various terms in the model equations represent advection, production, destruction and diffusion. The generation of turbulence due to small-scale turbulent fluctuations and the generation of laminar kinetic energy due to large-scale turbulent fluctuations are modelled as

$$P_{k_T} = \nu_{T,s} S^2 \,, \tag{15}$$
$$P_{k_L} = \nu_{T,l} S^2 \,, \tag{16}$$

where $S = \sqrt{2S_{ij}S_{ij}}$ is the mean strain-rate magnitude, $\nu_{T,s}$ and $\nu_{T,l}$ are the small-scale and large-scale components of the eddy-viscosity, respectively.

The small-scale eddy-viscosity is defined as

$$\nu_{T,s} = f_\nu f_{INT} C_\mu \sqrt{k_{T,s}} \lambda_{eff} \ , \tag{17}$$

where $k_{T,s}$ is the effective small-scale turbulence

$$k_{T,s} = f_{SS} f_W k_T \ . \tag{18}$$

The kinematic wall effect is included through an effective wall-limited turbulence length scale

$$\lambda_{eff} = \min\left(C_\lambda d, \lambda_T\right),$$

and damping function

$$f_W = \left(\frac{\lambda_{eff}}{\lambda_T}\right)^{\frac{2}{3}},$$

where

$$\lambda_T = \frac{\sqrt{k_T}}{\omega},$$

and d denotes the wall distance.

The viscous wall effect is incorporated through a viscous damping function

$$f_\nu = 1 - \exp\left(-\frac{\sqrt{Re_T}}{A_\nu}\right),$$

where

$$Re_T = \frac{f_W^2 k_T}{\nu\omega}$$

is the effective turbulence Reynolds number.

The shear-sheltering effect is included through the following damping function:

$$f_{SS} = \exp\left[-\left(\frac{C_{SS}\nu\Omega}{k_T}\right)^2\right] \ , \tag{19}$$

where $\Omega = \sqrt{2\Omega_{ij}\Omega_{ij}}$ is the vorticity magnitude.

In order to satisfy the realizability constraint suggested by Shih *et al.* [6], the turbulent viscosity coefficient, C_μ, takes the form

$$C_\mu = \frac{1}{A_0 + A_S\left(\frac{S}{\omega}\right)} \ . \tag{20}$$

Intermittency effects on the production of turbulence are included through the intermittency damping function

$$f_{INT} = \min\left(\frac{k_T}{C_{INT} k_{TOT}}\right) \ , \tag{21}$$

where $k_{TOT} = k_T + k_L$ is the total fluctuation kinetic energy.

The production of laminar kinetic energy, k_L, is assumed to be given by large-scale near wall turbulence, based on the correlation of pre-transitional fluctuation growth with free-stream

low-frequency wall-normal turbulent fluctuations [7]. The large-scale turbulence contribution is defined as

$$k_{T,l} = k_T - k_{T,s} \ , \tag{22}$$

whereas the small-scale contribution is defined by Eq. 18. The production term is then given by Eq. 15, where

$$\nu_{T,l} = \min \left\{ f_{\tau l} C_{l1} \left(\frac{\Omega \lambda_{eff}^2}{\nu} \right) \sqrt{k_{T,l}} \lambda_{eff} + \beta_{TS} C_{l2} Re_\Omega d^2 \Omega, \frac{k_L + k_{T,l}}{2S} \right\} , \tag{23}$$

where

$$\begin{aligned} Re_\Omega &= \frac{d^2 \Omega}{\nu} \ , \\ \beta_{TS} &= 1 - \exp \left(\frac{-\max \left(Re_\Omega - C_{TS,crit}, 0 \right)^2}{A_{TS}} \right) \ , \\ f_{\tau,l} &= 1 - \exp \left(-C_{\tau,l} \frac{k_{T,l}}{\lambda_{eff}^2 \Omega^2} \right) \ . \end{aligned}$$

The limit is applied to ensure satisfaction of the realizability constraint for the total Reynolds stress contribution. The production term is comprised of two parts: the first addresses the development of Klebanoff modes and the second addresses self-excited (*i.e.* natural) modes.

The dissipation is divided into an isotropic ($k_T \omega$) and an anisotropic (D_T and D_L) part, as in the low-Reynolds Launder-Sharma $k - \epsilon$ model [8], with

$$D_T = \nu \frac{\partial \sqrt{k_T}}{\partial x_i} \frac{\partial \sqrt{k_T}}{\partial x_i} \ , \tag{24}$$

$$D_L = \nu \frac{\partial \sqrt{k_L}}{\partial x_i} \frac{\partial \sqrt{k_L}}{\partial x_i} \ . \tag{25}$$

The turbulent transport terms in the k_T and ω equations include a turbulent effective diffusivity, α_T, defined as

$$\alpha_T = f_\nu C_{\mu,std} \sqrt{k_{T,s}} \lambda_{eff} \ . \tag{26}$$

The boundary layer production term, P_{BL}, is added to reproduce properly the behaviour of the boundary layer wake region, and is defined as:

$$P_{BL} = C_{\omega 3} f_\omega \alpha_T f_W^2 \frac{\sqrt{k_T}}{d^3} \ , \tag{27}$$

where

$$f_\omega = 1 - \exp \left[-0.41 \left(\frac{\lambda_{eff}}{\lambda_T} \right)^4 \right] \tag{28}$$

is the kinematic damping function.

The remaining terms in the transport equations are related to the laminr-turbulent transition mechanism in the model. As mentioned above, transition occurs as a transfer of energy from k_L

to k_T, with a concurrent reduction in turbulence length scale from the free-stream value to the value found in an equilibrium turbulent boundary layer.

The transport equation for turbulent kinetic energy, k_T, and the transport equation for laminar kinetic energy, k_L, are linked by the terms R_{BP} and R_{NAT}, which represent the break-down process of the pre-transitional fluctuations. Once a certain threshold is reached (β_{BP} and β_{NAT}), these terms become a sink to the k_L transport equation and a source to the k_T equation. R_{BP} and R_{NAT} account for the bypass and natural transition mechanism, respectively, and are defined as:

$$R_{BP} = C_R \beta_{BP} k_L \omega / f_W \ , \tag{29}$$

$$R_{NAT} = C_{R,NAT} \beta_{NAT} k_L \Omega \ , \tag{30}$$

where

$$\beta_{BP} = 1 - \exp\left(-\frac{\phi_{BP}}{A_{BP}} \right) \ , \tag{31}$$

$$\phi_{BP} = \max\left[\left(\frac{k_T}{\nu \Omega} - C_{BP,crit} \right), 0 \right] \ , \tag{32}$$

$$\beta_{NAT} = 1 - \exp\left(-\frac{\phi_{NAT}}{A_{NAT}} \right) \ , \tag{33}$$

$$\phi_{NAT} = \max\left(Re_\Omega - \frac{C_{NAT,crit}}{f_{NAT,crit}}, 0 \right) \ , \tag{34}$$

$$f_{NAT,crit} = 1 - \exp\left(-C_{NC} \frac{\sqrt{k_L} d}{\nu} \right) \ , \tag{35}$$

Transition in both cases is assumed to initiate when the characteristic time-scale for turbulence production is smaller than the viscous diffusion time-scale of the pre-transitional fluctuations.

The turbulent kinematic viscosity used in the momentum equations is the sum of the small-scale and large-scale contributions defined above

$$\nu_T = \nu_{T,s} + \nu_{T,l} \ . \tag{36}$$

When including heat transfer effects, the turbulent thermal diffusivity, α_θ, is modelled as

$$\alpha_\theta = f_W \frac{k_T}{k_{TOT}} \frac{\nu_{T,s}}{Pr} + (1 - f_W) \, C_{\alpha,\theta} \sqrt{k_T} \lambda_{eff} \ . \tag{37}$$

As regards the dissiparion rate transport equation, the first term on the right hand side of Eq. 6 represents an increase in dissipation rate due to turbulence production. The damping function of the third term is of the following form

$$f_2 = C_{\omega 2} f_W^2 \ , \tag{38}$$

while all the other model constants are reported in Tab. 1.

Table 1: Summary of model constants

$A_0 = 4.04$	$A_S = 2.12$	$A_\nu = 6.75$
$A_{BP} = 0.6$	$A_{NAT} = 200$	$A_{TS} = 200$
$C_{BP,crit} = 1.2$	$C_{NC} = 0.1$	$C_{NAT,crit} = 1250$
$C_{INT} = 0.75$	$C_{TS,crit} = 1000$	$C_{R,NAT} = 0.02$
$C_{l1} = 3.4 \times 10^{-6}$	$C_{l2} = 10^{-10}$	$C_R = 0.12$
$C_{\alpha,\theta} = 0.035$	$C_{SS} = 1.5$	$C_{\tau,l} = 4360$
$C_{\omega 1} = 0.44$	$C_{\omega 2} = 0.92$	$C_{\omega 3} = 0.3$
$C_{\omega R} = 1.5$	$C_\lambda = 2.495$	$C_{\mu,std} = 0.09$
$Pr = 0.85$	$\sigma_k = 1$	$\sigma_\omega = 1.17$

3 DG SPACE and TIME DISCRETIZATION

The governing equations can be written in compact form as

$$\frac{\partial \mathbf{q}}{\partial t} + \boldsymbol{\nabla} \cdot \mathbf{F}_c(\mathbf{q}) + \boldsymbol{\nabla} \cdot \mathbf{F}_v(\mathbf{q}, \boldsymbol{\nabla}\mathbf{q}) + \mathbf{s}(\mathbf{q}, \boldsymbol{\nabla}\mathbf{q}) = \mathbf{0}, \tag{39}$$

where $\mathbf{q} \in \mathbb{R}^m$ denotes the vector of the m primitive variables, $\mathbf{s} \in \mathbb{R}^m$ the source term, d the space dimension, $\mathbf{F}_c, \mathbf{F}_v \in \mathbb{R}^M \otimes \mathbb{R}^N$ the inviscid and viscous flux functions.

A weak formulation of Eq. (39) is obtained multiplying each scalar law by an arbitrary smooth test function $v_j \in \mathbf{v}$, $1 \leq j \leq m$, and integrating by parts:

$$\int_\Omega v_j \frac{\partial q_j}{\partial t} \, \mathrm{d}\mathbf{x} - \int_\Omega \boldsymbol{\nabla} v_j \cdot \mathbf{F}_j(\mathbf{q}, \boldsymbol{\nabla}\mathbf{q}) \, \mathrm{d}\mathbf{x} + \int_{\partial\Omega} v_j \mathbf{F}_j(\mathbf{q}, \boldsymbol{\nabla}\mathbf{q}) \cdot \mathbf{n} \, \mathrm{d}\sigma + \int_\Omega v_j \mathbf{s}_j(\mathbf{q}, \boldsymbol{\nabla}\mathbf{q}) \, \mathrm{d}\mathbf{x} = 0, \tag{40}$$

where $\mathbf{F}_j$ is the sum of the inviscid and viscous flux vectors, Ω the computational domain, $\partial\Omega$ the boundary of Ω, $\mathbf{n}$ the unit normal vector to the boundary.

Let Ω_h be an approximation of the domain $\Omega \in \mathbb{R}^d$, $\mathcal{T}_h = \{K\}$ a mesh of Ω_h, i.e. a collection of "finite elements" K, $\mathcal{F}_h = \{F\}$ the mesh faces, and let $\mathbf{V}_h$ denotes a discontinuous finite element space spanned by polynomial functions continuous only inside each element K, i.e.

$$\mathbf{V}_h \stackrel{\text{def}}{=} \left[\mathbb{P}_d^l(\mathcal{T}_h)\right]^m, \tag{41}$$

where

$$\mathbb{P}_d^l \stackrel{\text{def}}{=} \{v_h \in L^2(\Omega_h) : v_h|_K \in \mathbb{P}_d^l, \forall K \in \mathcal{T}_h\} \tag{42}$$

is the space of polynomials of degree at most l on the element K. Hierarchical and orthogonal shape functions are adopted and are obtained using a modified Gram-Schmidt procedure, assuming as a starting point a set of monomial functions [12]. The solution $\mathbf{q}$, the test function $\mathbf{v}$ are replaced with finite element approximations $\mathbf{q}_h$ and $\mathbf{v}_h$, belonging to the space $\mathbf{V}_h$. The DG

formulation of the problem (40) requires to find $\mathbf{q}_h \in \mathbf{V}_h$ such that

$$\sum_{K\in\mathcal{T}_h}\int_K v_{h,j}\frac{\partial q_{h,j}}{\partial t}\,\mathrm{d}\mathbf{x} - \sum_{K\in\mathcal{T}_h}\int_K \boldsymbol{\nabla}_h v_{h,j}\cdot\mathbf{F}_j\left(\mathbf{q}_h,\boldsymbol{\nabla}_h\mathbf{q}_h+\mathbf{r}(\llbracket\mathbf{q}_h\rrbracket)\right)\,\mathrm{d}\mathbf{x} + \sum_{F\in\mathcal{F}_h}\int_F \llbracket v_{h,j}\rrbracket\cdot\widehat{\mathbf{f}}_j\left(\mathbf{q}_h^{\pm},(\boldsymbol{\nabla}_h\mathbf{q}_h+\eta_F\mathbf{r}_F(\llbracket\mathbf{q}_h\rrbracket))^{\pm}\right)\,\mathrm{d}\sigma + \sum_{K\in\mathcal{T}_h}\int_K v_{h,j}\mathbf{s}_j\left(\mathbf{q}_h,\boldsymbol{\nabla}_h\mathbf{q}_h+\mathbf{r}(\llbracket\mathbf{q}_h\rrbracket)\right)\,\mathrm{d}\mathbf{x}=\mathbf{0} \qquad \mathbf{v}_h\in\mathbf{V}_h, \quad (43)$$

where $\mathbf{r}$ and $\mathbf{r}_F$ are the global and the local lifting operators, η_F a stability parameter, and $\widehat{\mathbf{f}}$ is the sum of the inviscid and the viscous numerical fluxes.

The numerical flux function $\widehat{\mathbf{f}}$, appearing in the boundary integral of Eq. (43), is introduced in order to uniquely define the flux at the elements interfaces, to obtain a consistent and conservative approximation of Eq. (40), and to prescribe the boundary data. The flux $\widehat{\mathbf{f}}$ is the sum of an inviscid, $\widehat{\mathbf{f}}_c$, and a viscous, $\widehat{\mathbf{f}}_v$, part. The former is based on the Godunov flux computed with an exact Riemann solver. For the latter the BR2 scheme, proposed in [11] and theoretically analyzed in [9, 10], is employed.

The DG space discretization of Eq. (43) results in the following system of (nonlinear) ODEs in time

$$\mathbf{M}\frac{d\mathbf{Q}}{dt}+\mathbf{R}\left(\mathbf{Q}\right)=0, \quad (44)$$

where $\mathbf{Q}$ is the global vector of unknown degrees of freedom, $\mathbf{M}$ is a global block diagonal matrix and $\mathbf{R}\left(\mathbf{Q}\right)$ is the vector of "residuals".

In the case of steady state computations the semi-discrete problem in Eq. (44) is discretized in time by means of the classical backward Euler scheme coupled with the pseudo-transient continuation strategy proposed in [14]. The resulting linear system is solved at each time step by means of GMRES algorithm. Linear algebra and parallelization are handled through PETSc library [13].

4 RESULTS

The implementation of the transition model was verified and assessed in the computation of two test cases, representative of the main transition modes: the compressible turbulent flow over a flat plate (T3A and T3B configurations of the ERCOFTAC SIG 10) and through the T106A turbine cascade. The influence of the polynomial degree, and of coarse grids on the solution accuracy were investigated, comparing results with available experimental data. All the computations were run in parallel, initializing the $\mathbb{P}^0$ solution from the uniform flow at inflow conditions and the higher-order solutions from the lower-order ones.

4.1 Zero-pressure-gradient flat plate

The transition model is first verified and validated on a zero-pressure-gradient flat plate. The T3A and T3B test cases of the ERCOFTAC were used, which are characterized by different values of the velocity and turbulence intensity at the leading edge, as reported in Tab. 2. Inlet turbulent quantities are chosen in order to match the value of Tu at the plate leading edge and the correct decay of the turbulence kinetic energy along the plate (see Tab. 3).

Table 2: Flow conditions of the T3A and T3B test cases

	T3A	T3B
Upstream Velocity (m/s)	5.4	9.4
Leading edge Tu (%)	3.0	6.0
Pressure Gradient	0	0

Table 3: Inlet turbulent quantities of the T3A and T3B test cases

	T3A	T3B
Tu_1	10%,	8.2%
$(\mu_T/\mu)_1$	0.35	114

In order to verify the implementation of the model, a grid sensitivity analysis was performed for the T3A test case on three meshes with 3600 (coarse), 8800 (medium) and 18000 (fine) quadrilateral elements. The solution approximations were $\mathbb{P}^{1\to4}$ for all the grids, while the maximum number of DoF was 54000 for the coarse mesh, 132000 for the medium mesh and 270000 for the fine mesh.

Figures 3a-3c show the skin friction coefficient, C_f, distributions on each mesh. In Fig. 3d a comparison of the predicted C_f distribution on the three meshes for the highest polynomial order with available experimental data [15], and with a standard k-$\widetilde{\omega}$ model is presented.

For every mesh, increasing the polynomial order of the solution approximation, all the predicted C_f curves are almost overlapped, and, starting from $\mathbb{P}^1$ approximation, the solution is in agreement with experimental data. Notice that the $\mathbb{P}^1$ solution on the coarse mesh corresponds only to 10800 DoF.

Also for the T3B test case, a grid sensitivity analysis was performed, using the same meshes (see Figs. 1 and 2).

Figures 4a-4c show the skin friction coefficient, C_f, distributions on each mesh. In Fig. 4d a comparison of the predicted C_f distribution on the three meshes for the highest polynomial order with available experimental data [15], and with a standard k-$\widetilde{\omega}$ model is presented. Also in this case the predicted curves are in good agreement with experimental data. The transition onset is slightly moved up, while the end of the transition is captured correctly.

For both test cases, the C_f distributions obtained with the standard k-$\widetilde{\omega}$ is also depicted in Figs. 3d and 4d, showing a completely wrong behaviour, *i.e.* a fast transition at the beginning of the plate.

4.2 MTU T106A

In this section the subsonic turbulent flow through the MTU T106A turbine cascade is considered. This cascade, designed by MTU Aero Engines, has been extensively investigated in experimental and computational studies [19, 18] and is characterized by a complex transitional turbulent flow.

An adiabatic wall boundary condition was imposed on blade surface. At the inflow, the total temperature, total pressure, flow angle $\alpha_1 = 37.7°$, and turbulence intensity $Tu_1 = 4\%$ were

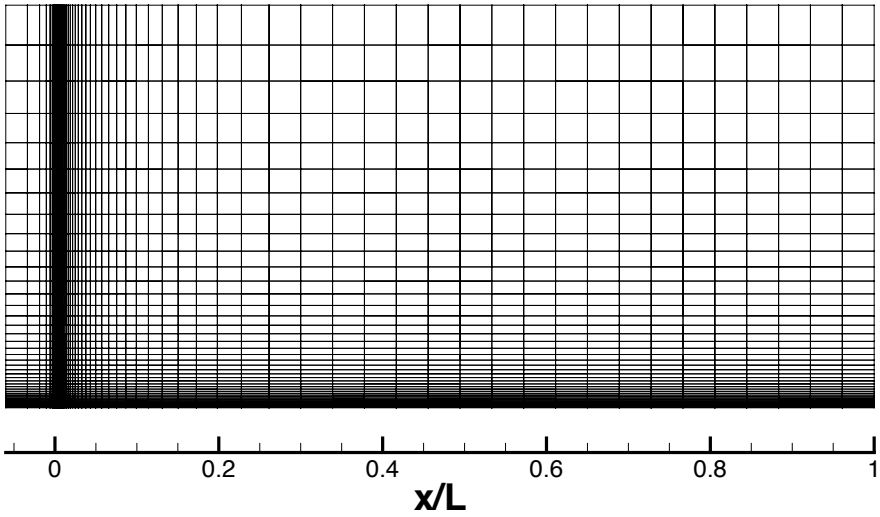

Figure 1: Flat plate - 3600 (coarse) quadrilateral elements mesh with linear edges for the flat plate test cases.

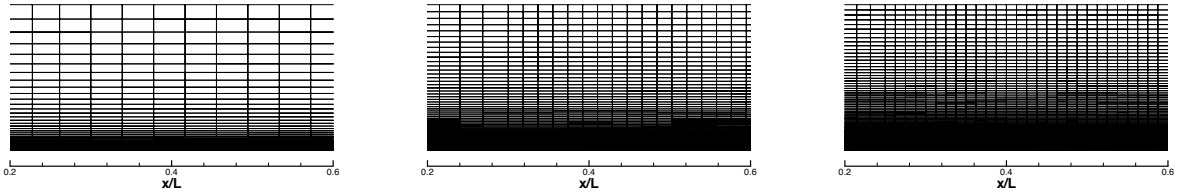

(a) Coarse (b) Medium (c) Fine

Figure 2: Flat plate - zoom in on the transition region for the coarse (a), medium (b), and fine (c) meshes.

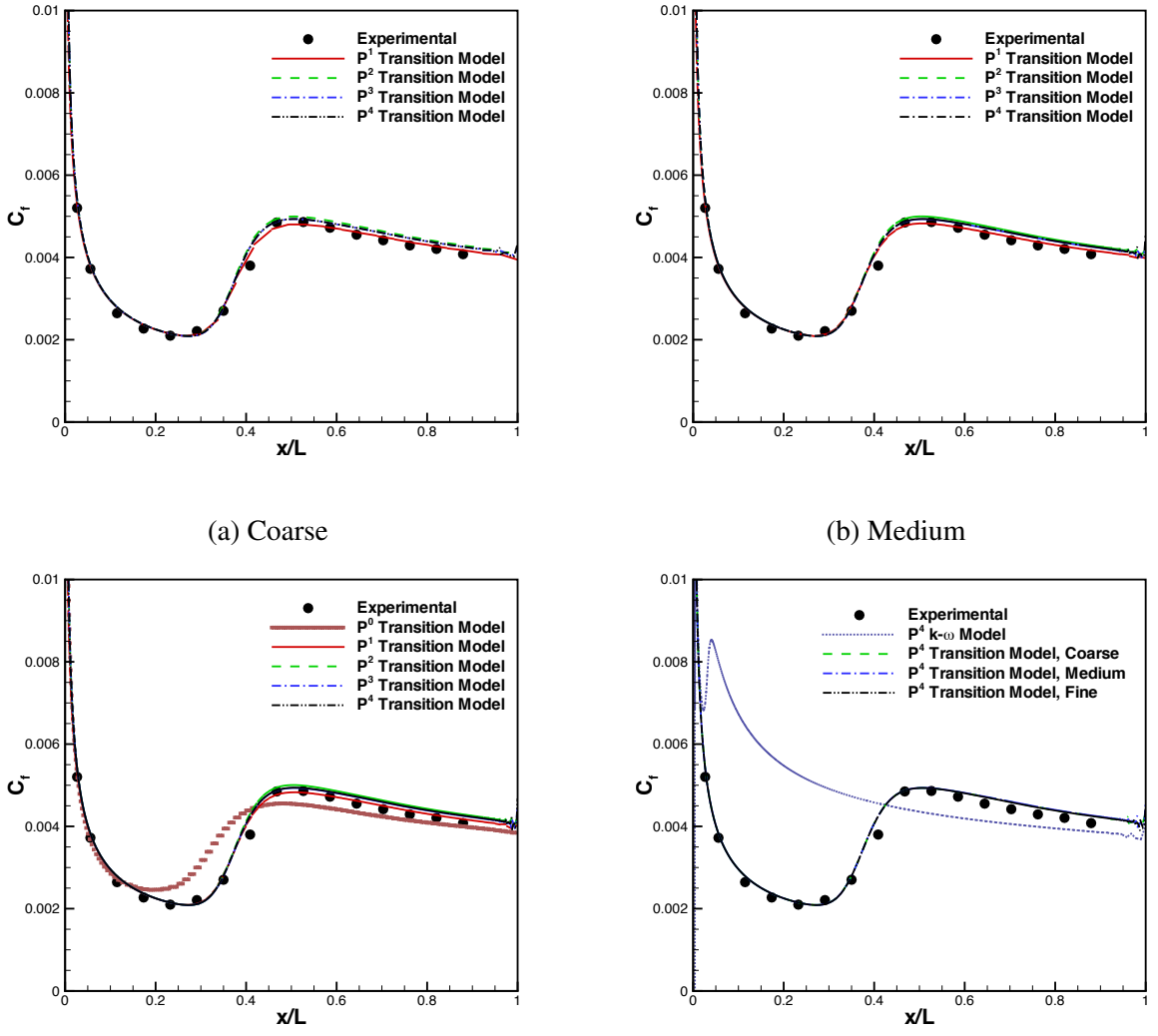

(a) Coarse

(b) Medium

(c) Fine

(d) Comparison

Figure 3: Flat plate T3A - distribution of the skin friction coefficient for the coarse (a), medium (b), fine (c) meshes, and comparison of the predicted skin friction distributions on the considered meshes for the highest polynomial order ($\mathbb{P}^4$) with a fully turbulent solution and experimental data (d).

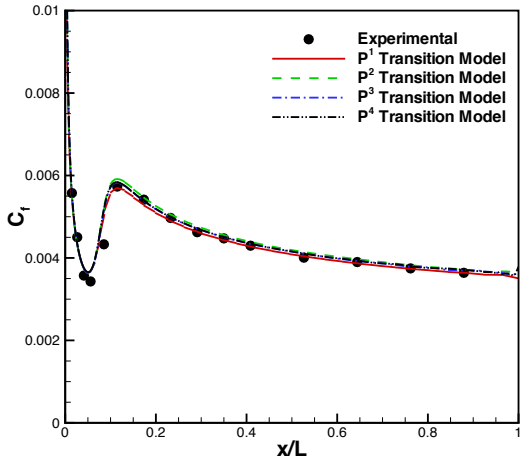

(a) Coarse

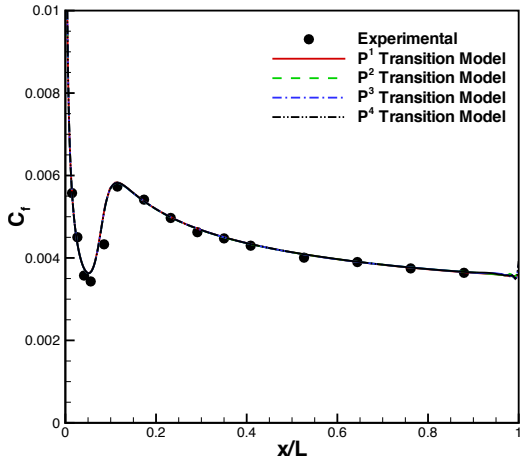

(b) Medium

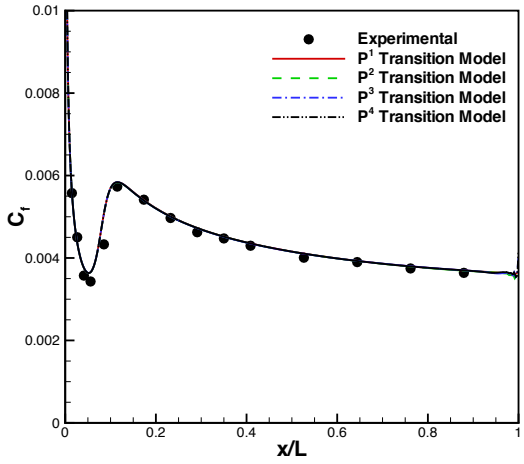

(c) Fine

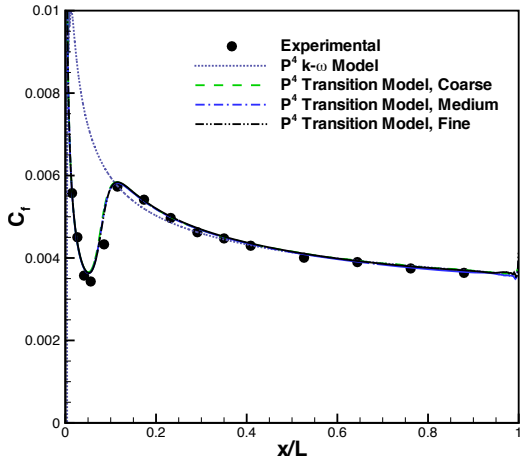

(d) Comparison

Figure 4: Flat plate T3B - distribution of the skin friction coefficient for the coarse (a), medium (b), fine (c) meshes, and comparison of the predicted skin friction distributions on the considered meshes for the highest polynomial order ($\mathbb{P}^4$) with a fully turbulent solution and experimental data (d)

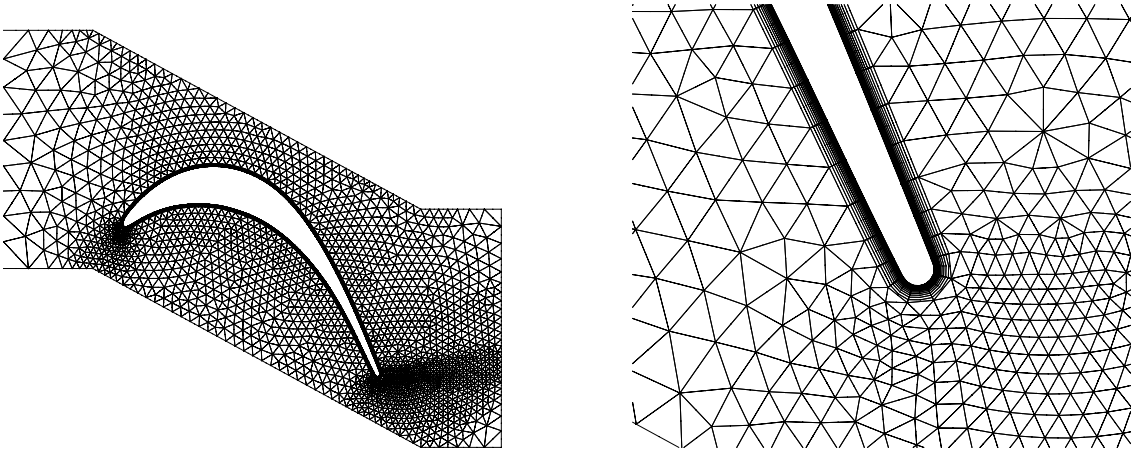

Figure 5: T106A, $Re_{2,is} = 1.1 \times 10^6$ - $y^+ = 5$ grid (left) and detail of the grid near the trailing edge (right)

prescribed. At the outflow, the static pressure was set, resulting in a downstream isentropic Mach number $M_{2,is} = 0.59$. The Reynolds number based on the downstream isentropic conditions and on the blade chord is $Re_{2,is} = 1.1 \times 10^6$. To assess the predicting capability of the model, the pressure coefficient, C_p, and the skin friction, C_f, distribution along the blade and the loss coefficient, ζ, were compared with experimental data. The flow field is attached for this flow condition and the prediction capabilities of the natural and bypass transition modes can be investigated.

All computations were performed by using a hybrid grid with a height of the first cell adjacent to the wall $y^+ = 5$ and 5743 quadratic elements. The grids employed for the simulations were generated with a 2D high-order version of a fully automated in-house hybrid mesh generator based on the advancing-Delaunay strategy [16]. The full grid and a detail of the trailing edge region can be seen in Fig. 5.

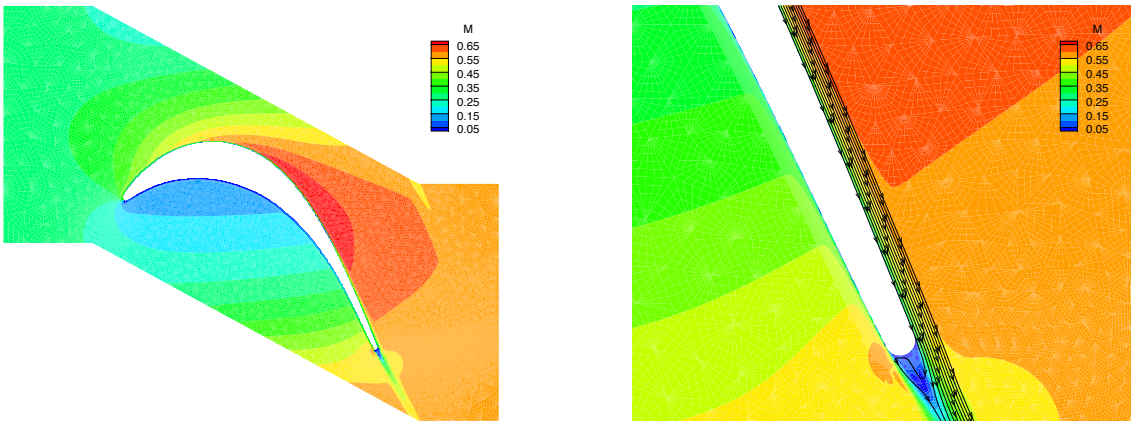

Figure 6: T106A, $Re_{2,is} = 1.1 \times 10^6$ - Mach number contours, $y^+ = 5$ grid, $\mathbb{P}^4$ approximation

Fig. 6 (left) shows the computed $\mathbb{P}^4$ Mach number contours on the $y^+ = 5$ mesh, while in Fig. 6 (right) the streamlines in the transition region confirms the absence of the flow separation.

Figure 7 shows the C_p distribution along the blade for $\mathbb{P}^{1\to4}$ approximation. Starting from $\mathbb{P}^2$ approximation, the curves on pressure and suction sides are in good agreement with the

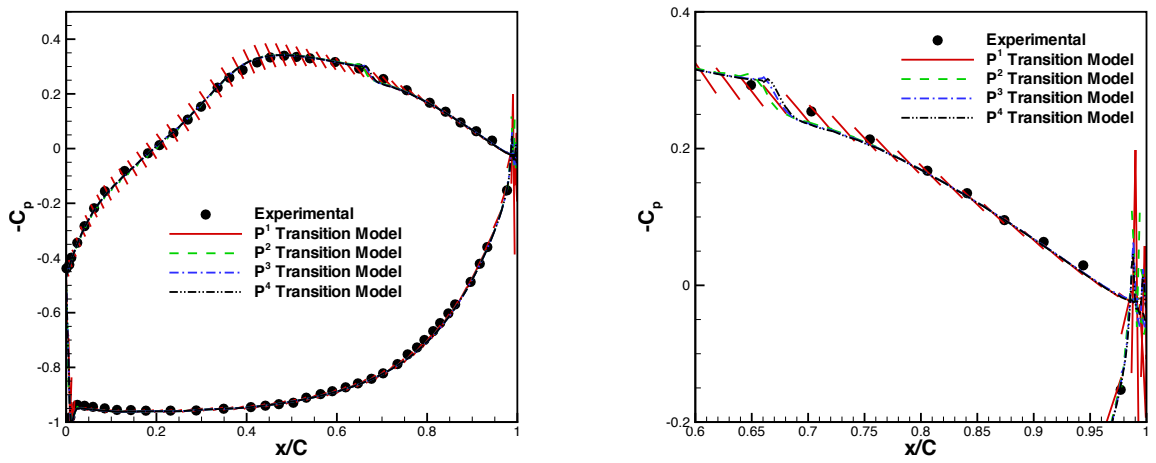

Figure 7: T106A, $Re_{2,is} = 1.1 \times 10^6$ - distribution of the pressure coefficient along the blade (left), and zoom in on the transition region (right), $y^+ = 5$ grid, $\mathbb{P}^{1\to4}$ approximations

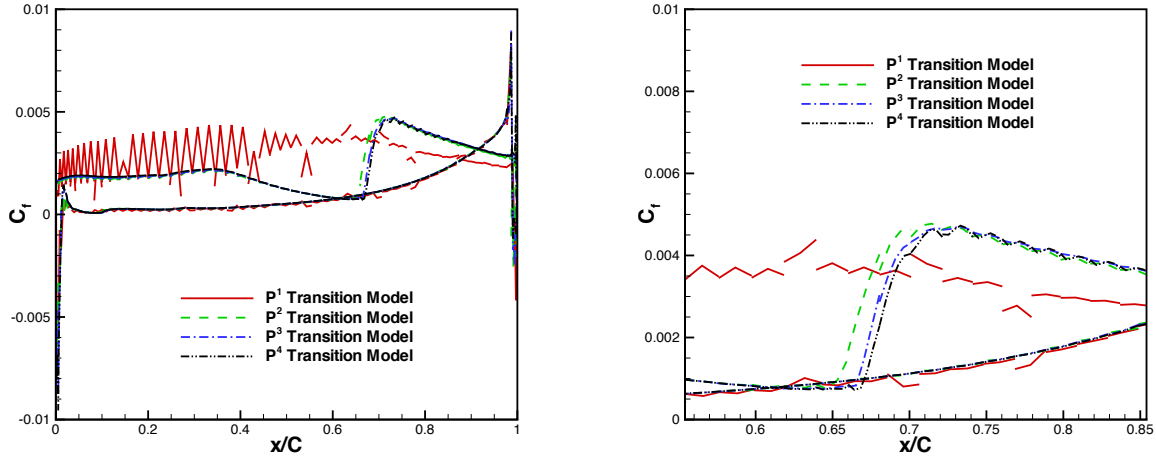

Figure 8: T106A, $Re_{2,is} = 1.1 \times 10^6$ - distribution of the skin friction coefficient along the blade (left), and zoom in on the transition region (right), $y^+ = 5$ grid, $\mathbb{P}^{1\to4}$ approximations

experimental data.

Fig. 8 shows the C_f distribution along the blade for all the polynomial approximations on the $y^+ = 5$ grid. The transition location moves slightly downstream, increasing the polynomial degree of the approximation. The $\mathbb{P}^1$ curve has rather large oscillations, which suggest that the spatial approximation need to be increased. Starting from $\mathbb{P}^2$ approximation, the transition location is predicted at approximately 65% of the chord, where a sudden increase of the C_f value can be observed.

Finally, in Tab. 4 the loss coefficient, ζ, is reported for each polynomial degree. As expected, it was overestimated by the low-order approximation, while the transition model allowed to predict almost the correct value starting from the $\mathbb{P}^2$ approximation.

5 CONCLUSIONS

The parallel implementation of a local transition model based on the laminar kinetic energy concept into a high-order accurate DG code was presented. The model was validated on the flat plate test case (T3A and T3B configurations) and we assessed the capability of the model to

Table 4: Loss coefficient, ζ, for the T106A test case.

	$\mathbb{P}^1$	$\mathbb{P}^2$	$\mathbb{P}^3$	$\mathbb{P}^4$	Experimental
$Re = 1.1 \times 10^6$, $y^+ = 5$	0.028	0.0204	0.0203	0.0202	0.02

compute complex transitional turbomachinery flows (MTU T106A turbine cascade). The beneficial effect of the transition model on the solution accuracy was demonstrated by comparing numerical results for increasing order of accuracy with fully turbulent solution and the available experimental data. Ongoing work is devoted to improve prediction capabilities of the transition model, considering also the laminar separation mode.

REFERENCES

[1] F.R. Menter, R.B. Langtry, S.R. Likki, Y.B. Suzen, P.G. Huang, S. Völker, A correlation-based transition model using local variables - Part I: Model formulation. *Journal of Turbomachinery*, **128**, 413–422, 2006.

[2] F.R. Menter, R.B. Langtry, S.R. Likki, Y.B. Suzen, P.G. Huang, S. Völker, A correlation-based transition model using local variables - Part II: Test cases and industrial applications. *Journal of Turbomachinery*, **128**, 423–434, 2006.

[3] D.K. Walters, D. Cokljat, A three-equation eddy-viscosity model for Reynolds-averaged Navier-Stokes simulations of transitional flow. *Journal of Fluids Engineering, Transactions of the ASME*, **130**, 121401-1–121401-14, 2008.

[4] F. Bassi, L. Botti, A. Colombo, A. Crivellini, C. De Bartolo, N. Franchina, A. Ghidoni, S. Rebay, Time integration in the discontinuous Galerkin code MIGALE – Steady problems. *Notes on Numerical Fluid Mechanics and Multidisciplinary Design*, **128**, 179–204, 2015.

[5] F. Bassi, L. Botti, A. Colombo, A. Crivellini, A. Ghidoni, A. Nigro, S. Rebay, Time integration in the discontinuous Galerkin code MIGALE – Unsteady problems . *Notes on Numerical Fluid Mechanics and Multidisciplinary Design*, **128**, 179–204, 2015.

[6] T.H. Shih, W.W. Liou, A. Shabbir, Z. Yang, J. Zhu, New k-eddy viscosity model for high Reynolds number turbulent flows. *Comput. & Fluids*, **24**, 227–238, 1995.

[7] R.J. Volino, T.W. Simon, Boundary Layer Transition Under High Free-Stream Turbulence and Strong Acceleration Conditions. *Journal of Turbomachinery*, **119**, 420–432, 1997.

[8] B.E. Launder, B.I. Sharma, Application of the Energy-dissipation Model of Turbulence to the Calculation of Flow Near a Spinning Disc. *Letters in Heat and Mass Transfer*, **2**, 131–138, 1974.

[9] F. Brezzi, G. Manzini, D. Marini, P. Pietra, A. Russo. Discontinuous Galerkin approximations for elliptic problems. *Numer. Methods Partial Differential Equations*, **16**, 365–378, 2000.

[10] D. N. Arnold, F. Brezzi, B. Cockburn, D. Marini. Unified analysis of discontinuous Galerkin methods for elliptic problems. *SIAM J. Numer. Anal.*, **39**, 1749–1779, 2002.

[11] F. Bassi, S. Rebay, G. Mariotti, S. Pedinotti, M. Savini. A high-order accurate discontinuous finite element method for inviscid and viscous turbomachinery flows. In: R. Decuypere and G. Dibelius. *Proceedings of the 2nd European Conference on Turbomachinery Fluid Dynamics and Thermodynamics*, Technologisch Instituut, Antwerpen, Belgium, 99–108, 1997.

[12] F. Bassi, L. Botti, A. Colombo, D. A. Di Pietro, P. Tesini. On the flexibility of agglomeration based physical space discontinuous Galerkin discretizations. *Journal of Computational Physics*, **231**, 45–65, 2012.

[13] S. Balay, K. Buschelman, W. D. Gropp, D. Kaushik, M. G. Knepley, L. C. McInnes, B. F. Smith, H. Zhang, 2001. PETSc Web page. Http://www.mcs.anl.gov/petsc.

[14] F. Bassi F, L. Botti, A. Colombo, A. Crivellini, N. Franchina, A. Ghidoni, S. Rebay. Very high-order accurate discontinuous Galerkin computation of transonic turbulent flows on aeronautical configurations. *ADIGMA - A European Initiative on the Development of Adaptive Higher-Order Variational Methods for Aerospace Applications*, *Notes on Numerical Fluid Mechanics and Multidisciplinary Design*, vol. 113, Kroll N, Bieler H, Deconinck H, Couaillier V, van der Ven H, Sørensen K (eds.). Springer Berlin / Heidelberg, 2010; 25–38.

[15] J. Coupland. ERCOFTAC Special Interest Group on Laminar to Turbulent Transition and Retransition: T3A and T3B test cases, *Technical Report*. ERCOFTAC, 1990.

[16] A. Ghidoni, E. Pelizzari, S. Rebay, V. Selmin, V. 3D anisotropic unstructured grid generation. *International Journal for Numerical Methods in Fluids*, **51**, 1097-1115, 2006.

[17] M. Lorini, F. Bassi, A. Colombo, A. Ghidoni. High-order implementation of a non-local transition model in a DG solver for turbomachinery applications. *Computers & Fluids*, **127**, 115-130, 2016.

[18] A. Ghidoni, A. Colombo, S. Rebay, F. Bassi. Simulation of the Transitional Flow in a Low Pressure Gas Turbine Cascade with a High-Order Discontinuous Galerkin Method. *Journal of Fluids Engineering*, **135**, 2012.

[19] H. Hoheisel. Entwicklung neuer Entwurfskonzepte fur zwei Turbinengitter, Teil III, Ergebnisse T106. *Technical Report*, Institut fur Entwurfsaerodynamik, Braunschweig,1981.